Journal of Thermal Analysis and Calorimetry (2020) 139:923–931
https://doi.org/10.1007/s10973-019-08518-9

Investigation on the structure, fluoride vaporization and crystallization behavior of CaF_2–CaO–Al_2O_3–(SiO_2) slag for electroslag remelting

Yu Liu[1,2] · Yong Wang[2] · Guangqiang Li[1,2,3] · Cheng Yuan[2] · Ru Lu[2] · Baokuan Li[4]

Received: 7 October 2018 / Accepted: 25 June 2019 / Published online: 2 July 2019

Abstract
The structure, vaporization behavior and crystallization of CaF_2–CaO–Al_2O_3 slags with different SiO_2 contents for electroslag remelting were investigated by employing the TG and DSC measurements in conjunction with the Raman spectroscopy measurement for linking the macroscopic physicochemical property and microstructure information. The results show that SiO_2 addition makes the depolymerized aluminate units polymerized into fully polymerized Q^4_{Al} unit and Al–O–Al complex structural groups. With the SiO_2 content increasing to 6.1 mass%, the vaporization rate of fluoride increases because the SiF_4 possessing higher vapor pressure is formed and the SiO_2 addition can promote the formation of AlF_3. As SiO_2 content is further increased to 8.6 mass%, the vaporization rate of fluoride decreases because the mass transfer becomes slower. The more complex slag structure resulted from SiO_2 addition dramatically decreases the crystallization temperature of the primary crystalline phase and the size of crystalline particles in the solidified slag.

Keywords SiO_2 addition · Slag structure · Vaporization · Crystallization · Electroslag remelting

Introduction

Electroslag remelting (ESR) is extensively applied in the manufacture of high-quality ingots used in critical applications such as tool, die or energy, heat- and pressure-resistant parts, which requires high-quality and defect-free metal [1–3]. It is well known that the metallurgical properties of slag are of vital importance to the ingots quality. During ESR, the role of the slag is to provide the following functions: (1) generate Joule heat for melting electrode, (2) refine liquid metal such as absorption of the harmful elements and non-metallic inclusions, (3) provide lubrication at solidifying steel shell/copper mold interface, (4) play an insulating role between the solidifying steel shell and mold, as so to prevent shunt effectively and improve electric efficiency, (5) control horizontal heat transfer between solidifying steel shell and mold [4–6]. The inappropriate horizontal heat transfer and/or poor lubrication performance of slag generally results in the surface defects on ingots. Horizontal heat transfer and lubrication performance of slag are strongly dependent on the crystallization characteristics of the slag [4, 7, 8]. The CaF_2–CaO–Al_2O_3 system with a small amount of MgO, SiO_2 or other components is widely used in ESR. In general, the presence of SiO_2 in the slag for electroslag remelting of high-Al and/or high-Ti steels should be avoided as much as possible because the SiO_2 as the reducible component in slag can react with Al or Ti in steel [9], and then, the cleanliness of steel deteriorates. Because of impurities in raw materials, it is very difficult and expensive to maintain very low SiO_2 content in slags during the practical ESR process. But for electroslag remelting of many steels, SiO_2 is an admissible component in slag [10], which can modify the

✉ Guangqiang Li
liguangqiang@wust.edu.cn

1 The State Key Laboratory of Refractories and Metallurgy, Wuhan University of Science and Technology, Wuhan 430081, China

2 Key Laboratory for Ferrous Metallurgy and Resources Utilization of Ministry of Education, Wuhan University of Science and Technology, Wuhan 430081, China

3 Collaborative Innovation Center of Steel Technology, University of Science and Technology Beijing, Beijing 100083, China

4 School of Metallurgy, Northeastern University, Shenyang 110004, China

characteristics of inclusions in steel and improve the lubrication performance of slag.

Many researches focused on the crystallization behaviors of conventional CaF_2–CaO–SiO_2-based slag system for continuous casting mold fluxes were carried out [11–15]. The continuous casting mold flux usually contains less than 10 mass% CaF_2, which is very different form the high-fluoride slag used in ESR. Shi et al. [4] studied that effect of SiO_2 on the crystallization behaviors of CaF_2–CaO–Al_2O_3 slags for ESR and found that a small amount of SiO_2 addition is favorable for providing sound lubrication. However, the effect of SiO_2 content on structure of CaF_2–CaO–Al_2O_3 molten slags that influence crystallization behavior and the microstructure of solidified slag has not been well studied. Furthermore, the SiO_2 can react with CaF_2 to form SiF_4, which will change the slag composition. In case of vacuum ESR, it is necessary to study the vaporization behavior of CaF_2–CaO–Al_2O_3 melted slags with SiO_2 addition. Fluoride emission from the slag melt is dependent on the slag viscosity and component activities [16–18], and the viscosity of slag is also affected by the structure [19]. Thus, the aim of the present study is to explore the underlying mechanism by which SiO_2 addition influences the structure, vaporization and crystallization behavior of CaF_2–CaO–Al_2O_3 slag for electroslag remelting. The microstructures and sizes of crystals of solidified slags with different SiO_2 contents were also compared to further understand the role of SiO_2 on the crystallization of CaF_2–CaO–Al_2O_3 slag.

Experimental

Preparation of slag

The reagent-grade powders of CaF_2, Al_2O_3 and SiO_2 were used in the present experiment. The CaO powders were obtained from the reagent-grade $CaCO_3$ that were calcined at 1273 K for 10 h in a muffle furnace. To avoid the hydrolysis of CaF_2 powders at high temperature, the CaF_2, Al_2O_3 and SiO_2 powders were heated to 573 K with 10-h holding for dehydration. Four types of slags with different SiO_2 content were accurately prepared by electronic balance with an accuracy of 0.1 mg, indicated as T0, T1, T2 and T3, respectively. The chemical compositions of these four designed slags are listed in Table 1. The well-blended powders were pre-melted at 1773 K for 5 min in a graphite crucible in the induction furnace in order to obtain homogeneous slag samples for experiment, and subsequently, the liquid samples were quenched on a copper plate. The quenched slag was then carefully crushed and ground. The chemical compositions of the pre-melted slag determined by X-ray fluorescence (XRF, ARL9900) spectroscopy are also listed in Table 1. To semi-quantitatively determine the various functional group structures of slag, the quenched slag was determined by using a laser confocal Raman spectrometer (Renishaw, RM2000). The Raman spectra were collected at room temperature in the range 100–2000 cm^{-1} using a laser source having wavelength 532 nm.

Table 1 Composition of slag used for the present experiment

Slag	Designed slag/mass%				Pre-melted slag/mass%			
	CaF_2	CaO	Al_2O_3	SiO_2	CaF_2	CaO	Al_2O_3	SiO_2
T0	33.3	33.3	33.4	0	33.3	33.4	33.3	0
T1	32.3	32.2	32.3	3.2	32.1	32.6	32.4	2.9
T2	31.3	31.2	31.2	6.3	28.8	33.6	31.5	6.1
T3	30.3	30.3	30.3	9.1	28.7	32.6	30.1	8.6

Experimental procedures

The thermo gravimetry (TG, Netzsch STA 449 C/6/G) measurements were taken in Ar gas atmosphere (Ar gas flow rate at 10 mL min^{-1}) to investigate the fluoride vaporization behavior of the slags. For each TG measurement, approximately 30 mg of slag sample was heated at a constant heating rate of 40 K min^{-1} from room temperature to 1673 K in a platinum crucible with a diameter of 6.7 mm and a height of 5 mm, and was maintained for 30 min. The holding time was set to 30 min because a longer holding time would result in a great change in the composition of the slag melt. During the experiment, the mass change of samples with time and temperature was recorded automatically. Subsequently, the liquid sample was cooled at a constant cooling rate of 30 K min^{-1} to the room temperature.

To investigate the crystallization behavior of the slags, the differential scanning calorimetry (DSC, Netzsch STA 449 C/6/G) measurements were taken in Ar gas atmosphere (Ar gas flow rate at 40 mL min^{-1}). Approximately 30 mg of slag sample was heated at a constant heating rate of 40 K min^{-1} from room temperature to 1673 K in a platinum crucible with a diameter of 6.7 mm and a height of 5 mm and was maintained for 3 min to homogenize its chemical composition. Subsequently, the liquid sample was cooled at a constant cooling rate to the room temperature. Three DSC measurements with cooling rate of 10 K min^{-1}, 20 K min^{-1} and 30 K min^{-1} were performed for each slag samples. During the experiment, the DSC signal with time and temperature were recorded automatically.

To identify the crystalline phase corresponding to exothermic peak on DSC curve with 30 K min^{-1} cooling

rate, about 7 g slag sample was melted in a graphite crucible and then cooled at a cooling rate of approximately 30 K min^{-1} to 1273 K by adjusting output power. To retain the phase of slag at elevated temperature, the slag was rapidly quenched by nitrogen gas. Subsequently, the phases and microstructures of solidified slag were analyzed by X-ray diffraction (XRD, X'Pert PRO MPD) with Cu-K_α radiation and field emission scanning electron microscope (FE-SEM, Nova 400 Nano) equipped with energy-dispersive spectrometer (EDS, Le350 PentaFETx-3), respectively.

Results and discussion

Effect of SiO_2 addition on the structure of CaF_2–CaO–Al_2O_3 slag for ESR

The Raman bands of CaF_2–CaO–Al_2O_3 slags with varying SiO_2 contents are shown in Fig. 1. It indicates that SiO_2 addition dramatically changes the spectral curve, and the wave peak of the spectral curve moves backward. With the addition of SiO_2, the relative intensity of Raman bands in the region 650–800 cm^{-1} gradually decreases, whereas that in the region 800–1000 cm^{-1} gradually increases. The band that centers at around 550 cm^{-1} is assigned to the transverse motion of bridged oxygen atoms within the Al–O–Al bond, which is attributed to a connected network of the alumina tetrahedral whose four oxygen atoms are in a bridging configuration [20–23]. Thus, an increase in the relative height of Raman band 550 cm^{-1} indicates the number of bridging oxygen increases and/or number of non-bridging oxygen (NBO) decreases. The Raman bands at 730 cm^{-1}, 780 cm^{-1} and 850 cm^{-1} are the Al–O stretching vibration in AlO_4 tetrahedral units with the NBO/Al = 2 (Q^2_{Al}, non-bridging oxygen per Al), NBO/Al = 1 (Q^3_{Al}) and NBO/Al = 0 (Q^4_{Al}), respective [19, 20]. The Raman bands in the region 850–880 cm^{-1}, 900–920 cm^{-1} and 950–1000 cm^{-1} are the stretching vibration of Si–O bonds with the NBO/Si = 4 (Q^0_{Si}, non-bridging oxygen per Si), NBO/Si = 3 (Q^1_{Si}) and NBO/Al = 2 (Q^2_{Si}), respective [19, 24–26]. To quantitatively analyze the structural changes of slags with varying SiO_2, the Raman spectrum was deconvoluted by Gaussian fitting [19, 26]. The deconvolution results of Raman spectra are shown in Fig. 2. According to the results of Gaussian fitting in Fig. 2, the relative abundance of the Q^n_i (i = Al and Si) units can be calculated out from the area fraction of the best-fitted Gaussian curves at the frequency for the symmetric stretching vibration of each Q^n_i units [19, 24–26]. Figure 3 shows the relative fraction of individual structural units and the relative intensity of Al–O–Al as a function of SiO_2 content. Figure 3a indicates that the fractions of depolymerized aluminate units (Q^2_{Al}, NBO = 2; Q^3_{Al}, NBO = 1) decrease, whereas the fraction of the fully polymerized aluminate unit (Q^4_{Al}, NBO = 0) and the relative intensity of the Al–O–Al network bond slightly increase with the increases in SiO_2 content, implying that the simple Q^2_{Al} and Q^3_{Al} units are polymerized into Q^4_{Al} unit and Al–O–Al complex structural groups. Figure 3b indicates that the fractions of Q^0_{Si}, Q^1_{Si} and Q^2_{Si} increase with the SiO_2 content. The SiO_2 acts as a network former, and the Si atoms are localized at the boundary of AlO_4 unit with various numbers of NBO in the alumina-rich calcium aluminosilicate melts [27, 28], and the relationship between the silicate and aluminate structural units can be expressed by Eq. (1) as follows [29]:

$$(\mathrm{Si{-}O{-}Si}) + (\mathrm{Al{-}NBO}) = (\mathrm{Al{-}O{-}Si}) + (\mathrm{Si{-}NBO}) \quad (1)$$

Thus, the fraction of Si–NBO increases with the increase in SiO_2 content, whereas the fraction of Al–NBO decreases. The SiO_2 addition increases the fraction of Q^4_{Al} unit and the relative intensity of the Al–O–Al network bond, implying an increase in the degree of the polymerization of the AlO_4 tetrahedral network and the number of bridging oxygen in the slag. The viscosity of slag is closely related to the structure, and the viscosity of slag can be predicted according the Zhang's model [30, 31], as shown in Fig. 4. It indicates that the viscosity of slag increases with the SiO_2 content increasing. This is because that SiO_2 addition increases the degree of the polymerization of the slag structures, which consequently makes the structural units of slag melts more complex, leading to the increase in the diffusion resistance of slag components.

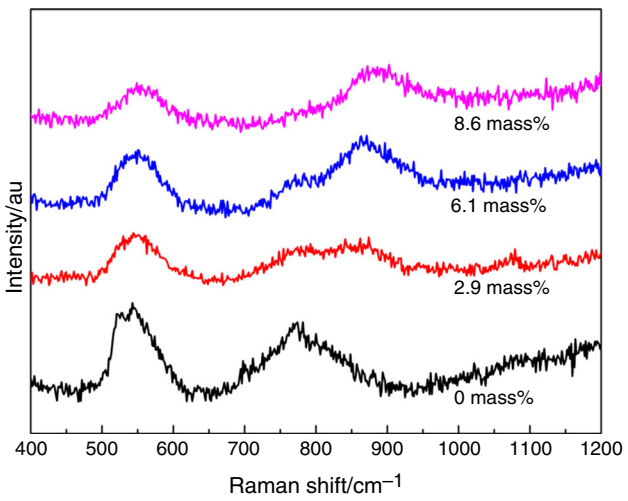

Fig. 1 Effect of SiO_2 content on Raman scattering of the CaF_2–CaO–Al_2O_3–SiO_2 system

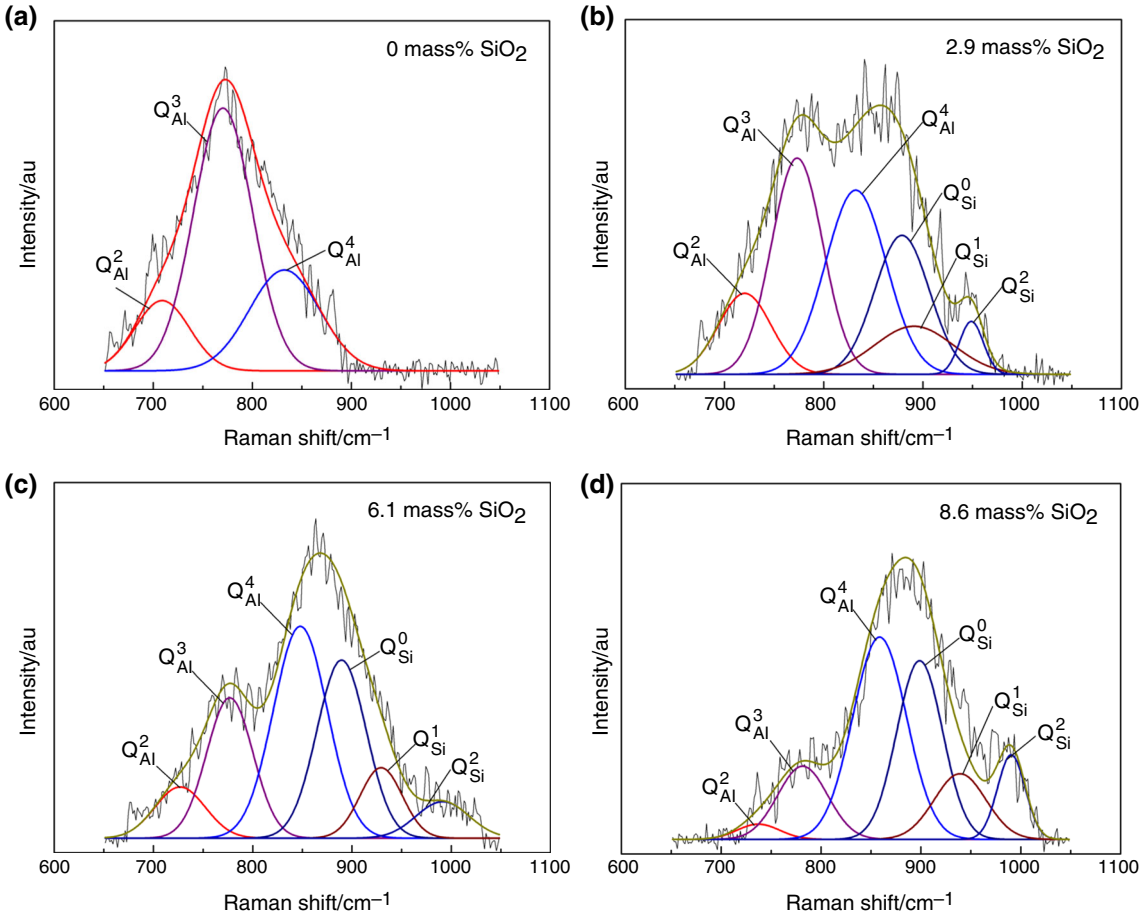

Fig. 2 Deconvoluted Raman spectra of the CaF_2–CaO–Al_2O_3–SiO_2 system with varying SiO_2 contents

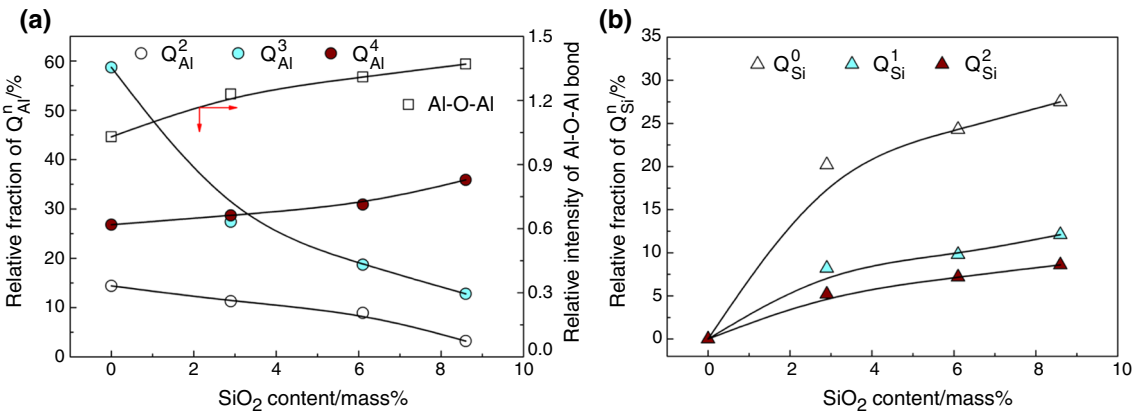

Fig. 3 Relative fraction of Qn i (n = 0 to 4, i = Al (**a**) or Si (**b**)) structure units and relative intensity of Al–O–Al bond (**a**) in the CaF_2–CaO–Al_2O_3–SiO_2 system as a function of SiO_2 content

Effect of SiO_2 addition on the vaporization behavior of CaF_2–CaO–Al_2O_3 slag for ESR

The mass loss can be expressed as:

$$\Delta m/m_0 = (m_t - m_0)/m_0 \quad (2)$$

where m_0 represents the initial mass of the slag sample and m_t is the mass of the slag sample at time t. Mass loss in the slag melts with varying SiO_2 contents at 1673 K is shown in Fig. 5. It indicates that the vaporization rate firstly increases from 7.81×10^{-6} to 1.32×10^{-5} s^{-1} with the SiO_2 content increasing from 0 to 6.1 mass% and then

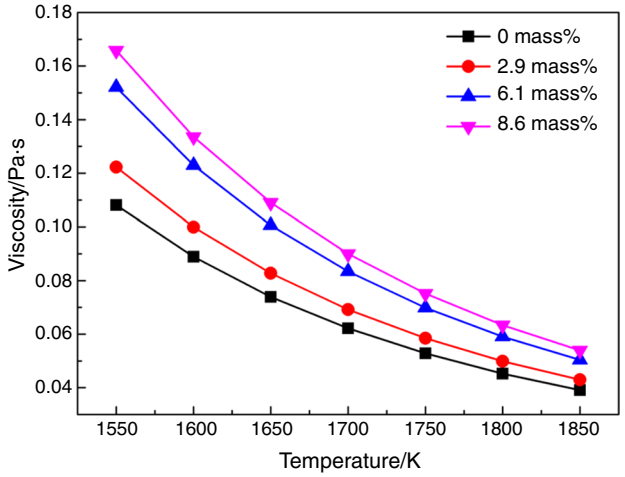

Fig. 4 The change of calculated viscosity with the temperature in the slag melts with varying SiO_2 contents

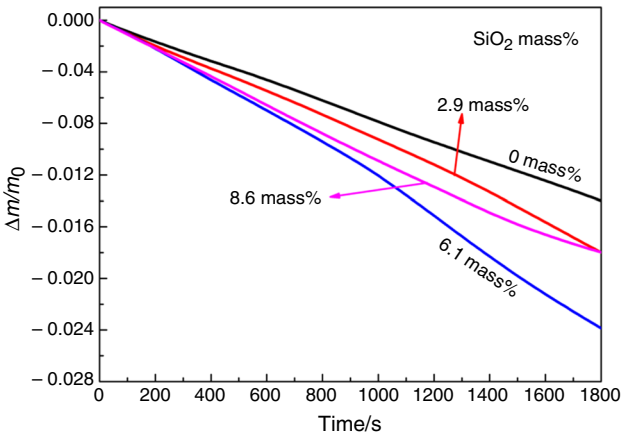

Fig. 5 Mass loss in the slag melts with varying SiO_2 contents at 1673 K

decreases from 1.32×10^{-5} to 9.98×10^{-6} s^{-1} as the SiO_2 content is further increased to 8.6 mass%. In the present study, there are two possible chemical reactions that cause the mass loss of the slag as follows [5]:

$$3(CaF_2) + (Al_2O_3) = 3(CaO) + 2\{AlF_3\} \quad (3)$$

$$2(CaF_2) + (SiO_2) = 2(CaO) + \{SiF_4\} \quad (4)$$

where { } indicates gas phase. In order to better understand the vaporization behavior of the fluoride-containing slag from the view of thermodynamics, the activities of components in slag melts at 1673 K were calculated on the basis of ion and molecule coexistence theory (IMCT) that were widely used for high-CaF_2 content-bearing slag [32–37]. The calculated activities of components in four types of slag melts at 1673 K are listed in Table 2. It indicates that the addition of SiO_2 increases the activities of CaF_2, Al_2O_3 and SiO_2, but decreases the activity of CaO.

Table 2 The activities of components in four types of slag melts at 1673 K calculated by IMCT

Slag	CaF_2	CaO	Al_2O_3	SiO_2
T0	0.6434	0.2106	0.0209	0
T1	0.6545	0.1766	0.0250	< 0.0001
T2	0.6422	0.1541	0.0289	0.0001
T3	0.6603	0.1195	0.0344	0.0001

The equilibrium constant (K) of reaction (3) can be expressed as:

$$K = \frac{a^3_{(CaO)} \cdot \left[\frac{p_{(AlF_3)}}{p^0}\right]^2}{a^3_{(CaF_2)} \cdot a_{(Al_2O_3)}} \quad (5)$$

where a (i) represents the activity of component i in slag, p (AlF_3) is the vapor pressure of the AlF_3, and p^0 is the standard atmospheric pressure. According to Eq. (5), the vapor pressure of the AlF_3 can be expressed as follows:

$$\lg\left[\frac{p_{(AlF_3)}}{p^0}\right] = \frac{1}{2}\lg K + \frac{1}{2}\lg\frac{a_{(Al_2O_3)} \cdot a^3_{(CaF_2)}}{a^3_{(CaO)}} \quad (6)$$

The change of $\frac{a_{(Al_2O_3)} \cdot a^3_{(CaF_2)}}{a^3_{(CaO)}}$ with the SiO_2 content calculated with IMCT in the slag at 1673 K is shown in Fig. 6. It indicates that $\frac{a_{(Al_2O_3)} \cdot a^3_{(CaF_2)}}{a^3_{(CaO)}}$ increases with the addition of SiO_2, implying that the SiO_2 addition can promote the formation of AlF_3. It is well known that SiO_2 enhances the vaporization of fluoride-containing slag due to the relatively high vapor pressure of SiF_4 [5, 6]. However, the role of SiO_2 in the formation of AlF_3 by reaction (3) has not been studied. In the present study, the thermodynamic

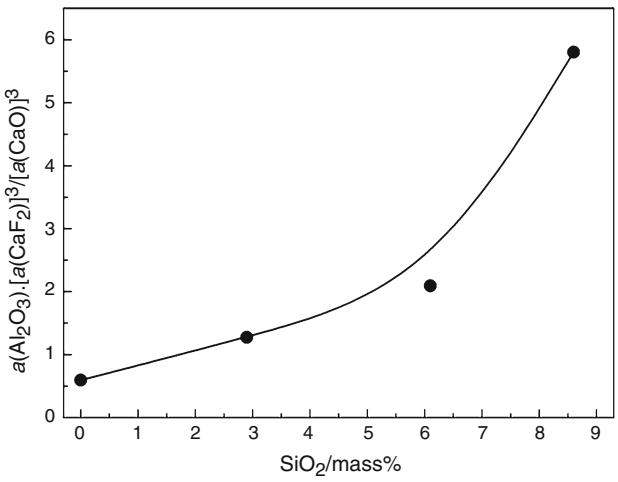

Fig. 6 Change of activity product with the SiO_2 content in the slag melts at 1673 K

calculation shows that SiO_2 addition can promote the formation of AlF_3. The vaporization rate increases from 7.81×10^{-6} to 1.32×10^{-5} s^{-1} with the SiO_2 content increasing from 0 to 6.1 mass% because the SiF_4 has higher vapor pressure and formation of AlF_3 is promoted.

As SiO_2 content is further increased to 8.6 mass%, the structural units of slag melts become more complex and the viscosity of slag melts increases (Figs. 3 and 4), which increases the diffusion resistance of slag components. Thus, the mass transfer for reactions (3) and (4) becomes slower and the vaporization rate decreases.

Effect of SiO_2 addition on the crystallization of CaF_2–CaO–Al_2O_3 slag for ESR

Figure 7 shows DSC curves of non-isothermal crystallization of slag melts at various cooling rates. There are two exothermic peaks on the DSC curves for each slag sample, implying the formation of two crystalline phases during the continuous cooling process (indicated as P1 and P2). The CCT curves of crystalline phase formation in slag melts are plotted according to the DSC results, as shown in Fig. 8. It indicates that SiO_2 addition dramatically decreases the crystallization temperatures of the crystalline phase. In the compositional range of slag used in the present experiment, the crystallization temperature of the first crystalline phase (indicated as P1 in Fig. 7) keeps decreasing with increase in SiO_2 content (Fig. 8a), whereas the further addition of SiO_2 has little effect on the crystallization temperature of the second crystalline phase (indicated as P2 in Fig. 7) when the SiO_2 content exceeds 2.9 mass% (Fig. 8b). As mentioned in "Effect of SiO_2 addition on the structure of CaF_2–CaO–Al_2O_3 slag for ESR" section, the SiO_2 addition increases the degree of the polymerization of the slag structures. An increase in the diffusion resistance of slag components results in an

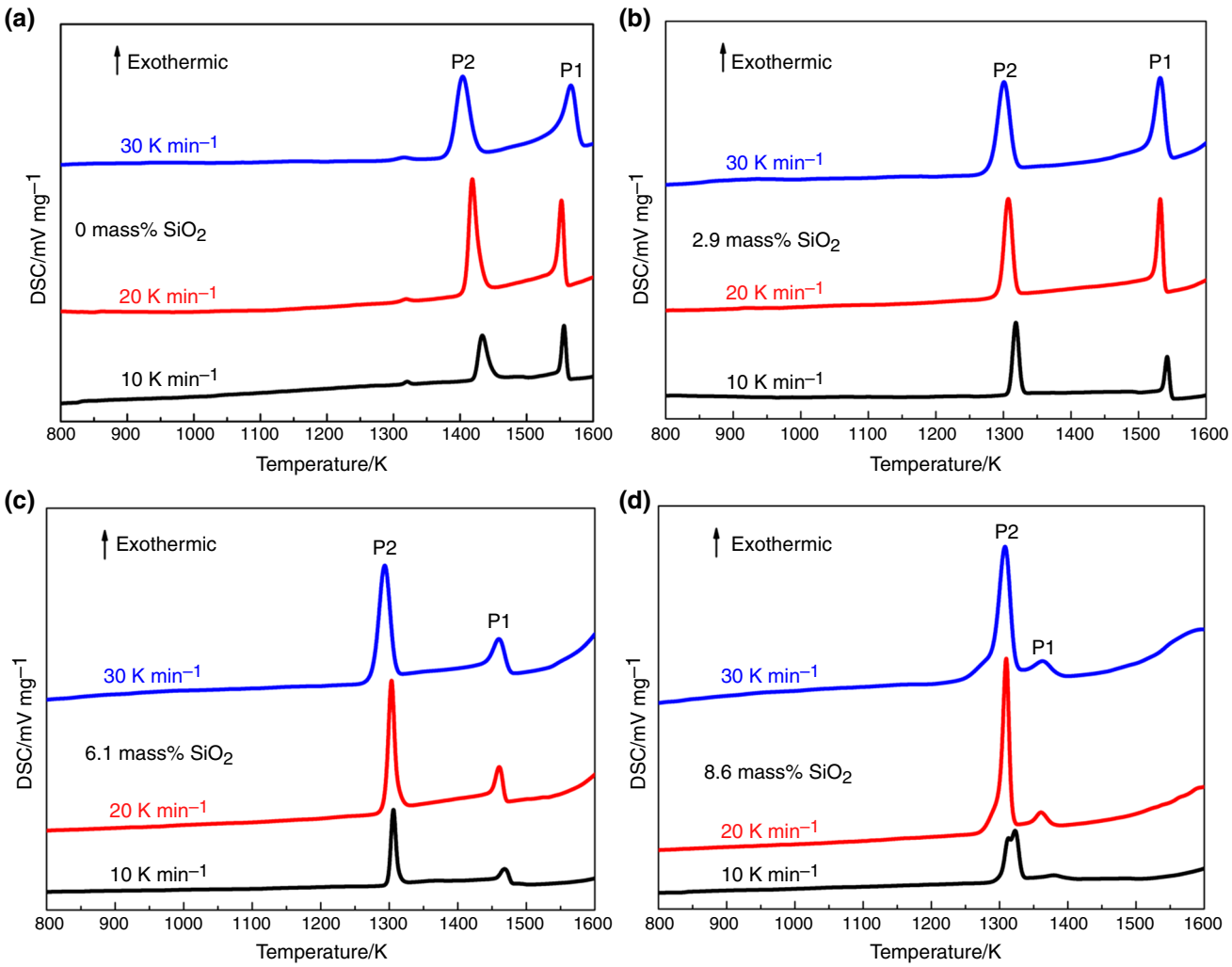

Fig. 7 DSC curves of non-isothermal crystallization of slag melts at various cooling rates: **a** slag T0 bearing 0 mass% SiO_2, **b** slag T1 bearing 2.9 mass% SiO_2, **c** slag T2 bearing 6.1 mass% SiO_2 and **d** slag T3 bearing 8.6 mass% SiO_2

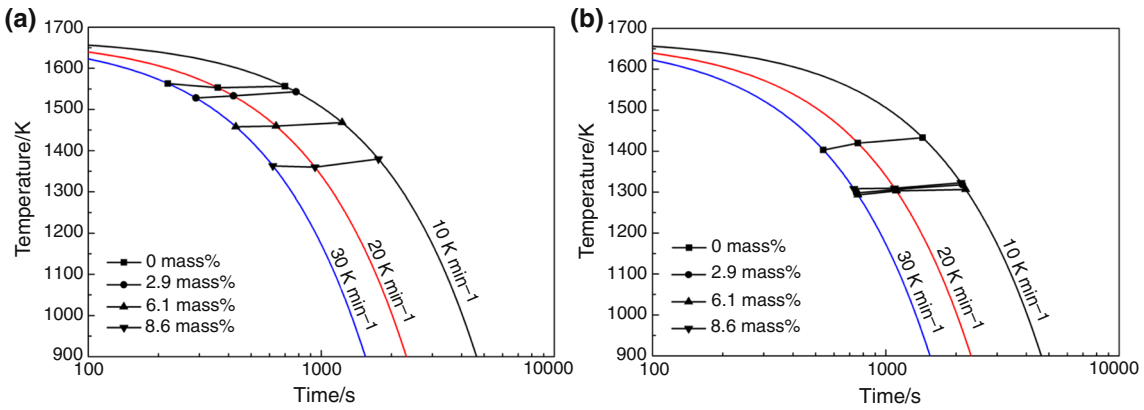

Fig. 8 CCT curves of crystalline phase formation in slag melts: **a** first crystalline phase and **b** second crystalline phase

increase in the time needed for crystallizations. Hence, crystallization temperature decreases with increase in SiO_2 content. The second crystalline phase forms at relatively lower temperature (Fig. 7), and the diffusion of the slag components has become very slow. As a result, further addition of SiO_2 does not obviously decrease the crystallization temperature of second crystalline phase. The SiO_2 addition greatly decreases the crystallization temperatures, which will contribute to the horizontal heat transfer and lubrication between solidifying steel shell and mold wall during ESR process.

XRD patterns of the slags bearing 0 mass% and 8.6 mass% SiO_2 quenched from the temperatures below 1273 K corresponding to the cooling rate of 30 K min^{-1} are shown in Fig. 9. It indicates that the two crystalline phases are $11CaO{\cdot}7Al_2O_3{\cdot}CaF_2$ and CaF_2, which well agrees with previous results [4]. According to the phase diagram of the $CaO–Al_2O_3–CaF_2$ and the previous analysis

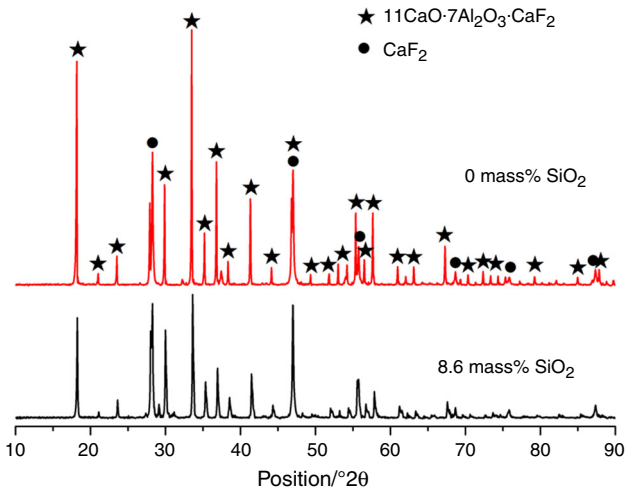

Fig. 9 XRD patterns of the slags bearing 0 mass% and 8.6 mass% SiO_2 cooled to below 1273 K at a cooling rate of 30 K min^{-1} and then quenched

[4, 38], the first and second crystalline phases are $11CaO{\cdot}7Al_2O_3{\cdot}CaF_2$ and CaF_2, respectively. To study the distribution of the crystalline phases, the EDS analysis was carried out. Corresponding elemental mappings indicate that the $11CaO{\cdot}7Al_2O_3{\cdot}CaF_2$ is the dominant crystalline phase (Fig. 10), which is consistent with the XRD analysis (Fig. 9).

The microstructures of solidified slags with 0 and 8.6 mass% SiO_2 content were also analyzed by SEM, as shown in Fig. 11. It indicates that there are many large crystalline particles (P1 and P2) in the solidified slag without SiO_2 (Fig. 11a), whereas the crystalline particles in the solidified slag with 8.6 mass% SiO_2 are finer (Fig. 11b). The more complex slag structure makes the mass transfer slower; namely, the growth of crystalline particle is slower. Furthermore, the SiO_2 addition decreases the crystallization temperature, and the diffusion rate will become slower at lower temperature. As a result, the finer crystalline particles are formed in the solidified slag with 8.6 mass% SiO_2. Thus, compared with the solidified slag with 8.6 mass% SiO_2, the more holes and cracks are observed in solidified slag without SiO_2.

Conclusions

The following conclusions can be drawn from the present study:

1. The SiO_2 acts as a network former in the simple Q^2_{Al} and Q^3_{Al} units by forming Al–O–Al complex structural groups and fully polymerized Q^4_{Al}. With the SiO_2 addition, the degree of the polymerization of the slag structures increases, which consequently makes the structural units of slag melts more complex, leading to the increase in the viscosity of $CaF_2–CaO–Al_2O_3$ slag melts and the diffusion resistance of slag components.

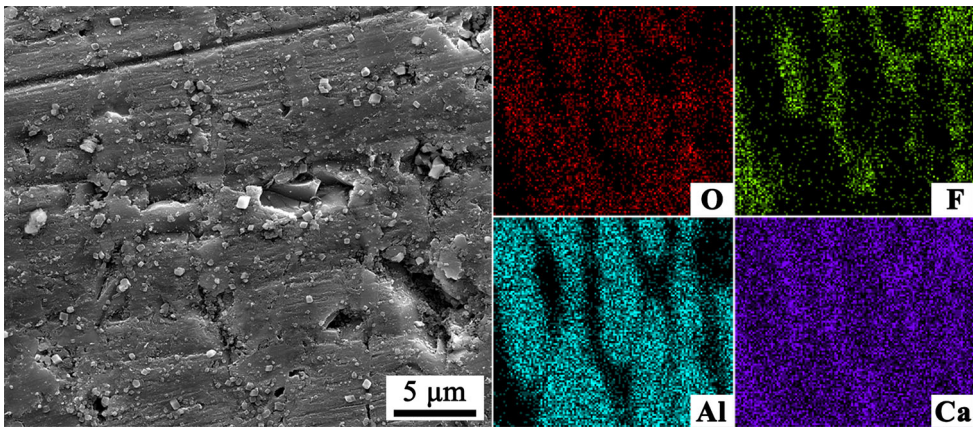

Fig. 10 Element mappings of the slag T0 cooled to below 1273 K at a cooling rate of 30 K min^{-1} and then quenched

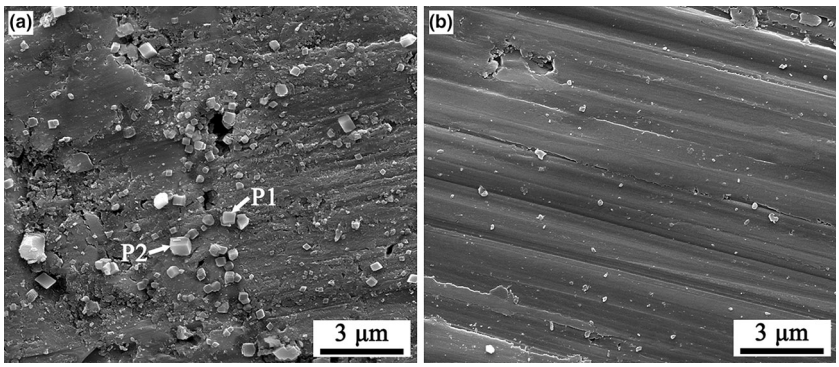

Fig. 11 SEM images of **a** the slag T0 and **b** slag T3 cooled to below 1273 K at a cooling rate of 30 K min^{-1} and then quenched

2. With the SiO_2 content increasing to 6.1 mass%, the vaporization rate of fluoride increases because the SiF_4 possessing higher vapor pressure is formed and the SiO_2 addition can promote the formation of AlF_3. As SiO_2 content is further increased to 8.6 mass%, the vaporization rate of fluoride decreases because the diffusion resistance of slag components for reaction of fluoride formation increases.
3. The crystallization temperature of CaF_2–CaO–Al_2O_3 slag decreases with the increase in SiO_2 content because the SiO_2 addition increases the diffusion resistance of slag components and the time needed for crystallization increases. Furthermore, the crystalline particles in the solidified slag become finer with the SiO_2 addition.

Acknowledgements The authors gratefully acknowledge the support from the Key Program of Joint Funds of the National Natural Science Foundation of China and the Government of Liaoning Province (Grant No. U1508214) and the National Natural Science Foundation of China (Grant No. 51210007).

References

1. Li B, Wang Q, Wang F, Chen M. A coupled cellular automaton-finite-element mathematical model for the multiscale phenomena of electroslag remelting H13 die steel ingot. JOM. 2014;66:1153–65.
2. Liu Y, Zhang Z, Li G, Wang Q, Wang L, Li B. Evolution of desulfurization and characterization of inclusions in dual alloy ingot processed by electroslag remelting. Steel Res Int. 2017;88:e201700058. https://doi.org/10.1002/srin.201700058.
3. Liu Y, Wang X, Li G, Wang Q, Zhang Z, Li B. Role of vacuum on cleanliness improvement of steel during electroslag remelting. Vacuum. 2018;154:351–8.
4. Shi CB, Li J, Cho JW, Jiang F, Jung IH. Effect of SiO_2 on the crystallization behaviors and in-mold performance of CaF_2–CaO–Al_2O_3 slags for drawing-ingot-type electroslag remelting. Metall Mater Trans B. 2015;46:2110–20.
5. Jiang ZH. Electroslag metallurgy. Beijing: Science Press; 2015.
6. Li ZB. Electroslag metallurgy theory and practice. Beijing: Metallurgical Industry Press; 2010.
7. Zheng DL, Li J, Shi CB, Ju JT. Effect of TiO_2 on the crystallisation behaviour of CaF_2–CaO–Al_2O_3–MgO slag for electroslag remelting of Ti-containing tool steel. Ironmak Steelmak. 2016;45:135–44.
8. Shi CB, Cho J, Zheng DL, Li J. Fluoride evaporation and crystallization behavior of CaF_2–CaO–Al_2O_3–(TiO_2) slag for electroslag remelting of Ti-containing steels. Int J Min Met Mater. 2016;23:627–36.
9. Liu Y, Li G, Wang L, Zhang Z. Effect of the tundish gunning materials on the steel cleanliness. High Temp Mater Proc. 2018;37:1–11.
10. Allibert M, Wadier J, Mitchell A. Use of SiO sub 2-containing slags in electroslag remelting. Ironmak Steelmak. 1978;5:211–6.
11. Zhou L, Wang W, Ma F, Li J, Wei J, Matsuura H. A kinetic study of the effect of basicity on the mold fluxes crystallization. Metall Mater Trans B. 2012;43:354–62.

12. Kashiwaya Y, Cicutti CE, Cramb AW. An investigation of the crystallization of a continuous casting mold slag using the single hot thermocouple technique. ISIJ Int. 1998;38:357–65.
13. Lu B, Wang W, Li J, Zhao H, Huang D. Effects of basicity and B_2O_3 on the crystallization and heat transfer behaviors of low fluorine mold flux for casting medium carbon steels. Metall Mater Trans B. 2013;44:365–77.
14. Watanabe T, Hashimoto H, Hayashi M, Nagata K. Effect of alkali oxides on crystallization in $CaO–SiO_2–CaF_2$ glasses. ISIJ Int. 2008;48:925–33.
15. Dubrawski J, Camplin J. Crystallization of mould powders used in the continuous casting of steel. J Therm Anal Calorim. 1993;40:329–34.
16. Persson M, Seetharaman S, Seetharaman S. Kinetic studies of fluoride evaporation from slags. ISIJ Int. 2007;47:1711–7.
17. Brandaleze E, Valentini M, Santini L, Benavidez E. Study on fluoride evaporation from casting powders. J Therm Anal Calorim. 2018;133:271–7.
18. Liu Y, Zhang Z, Li G, Wu Y, Xu D, Li B. Investigation of fluoride vaporization from $CaF_2–CaO–Al_2O_3$ slag for vacuum electroslag remelting. Vacuum. 2018;158:6–13.
19. Kim TS, Park JH. Structure–viscosity relationship of low-silica calcium aluminosilicate melts. ISIJ Int. 2014;54:2031–8.
20. Mcmillan P, Piriou B. Raman spectroscopy of calcium aluminate glasses and crystals. J Non Cryst Solids. 1983;55:221–42.
21. Shi C, Zheng D, Shin S, Li J, Cho J. Effect of TiO_2 on the viscosity and structure of low-fluoride slag used for electroslag remelting of Ti-containing steels. Int J Min Met Mater. 2017;24:18–24.
22. Licheron M, Montouillout V, Millot F, Neuville DR. Raman and ^{27}Al NMR structure investigations of aluminate glasses: $(1 - x)Al_2O_3–xMO$, with M = Ca, Sr, Ba and $0.5 < x < 0.75$. J Non-Cryst Solids. 2011;357:2796–801.
23. Higby PL, Ginther RJ, Aggarwal ID, Friebele EJ. Glass formation and thermal properties of low-silica calcium aluminosilicate glasses. J Non Cryst Solids. 1990;126:209–15.
24. Hyun PJ. Structure–property correlations of $CaO–SiO_2–MnO$ slag derived from Raman spectroscopy. ISIJ Int. 2012;52:1627–36.
25. Hyun PJ. Composition-structure-property relationships of $CaO–MO–SiO_2$ ($M = Mg^{2+}$, Mn^{2+}) systems derived from micro-Raman spectroscopy. J Non Cryst Solids. 2012;358:3096–102.
26. Park JH. Structure–property relationship of $CaO–MgO–SiO_2$ slag: quantitative analysis of Raman spectra. Metall Mater Trans B. 2013;44:938–47.
27. Mills K, Guo M. The importance of materials properties in high-temperature processes. ISIJ Int. 2014;54:2000–7.
28. Neuville DR, Cormier L, Flank AM, Briois V, Massiot D. Al speciation and Ca environment in calcium aluminosilicate glasses and crystals by Al and Ca K-edge X-ray absorption spectroscopy. Chem Geol. 2004;213:153–63.
29. Allwardt JR, Lee SK, Stebbins JF. Bonding preferences of non-bridging O atoms: evidence from ^{17}O MAS and 3QMAS NMR on calcium aluminate and low-silica Ca-aluminosilicate glasses. Am Mineral. 2003;88(7):949–54.
30. Zhang GH, Chou KC, Mills K. Modelling viscosities of $CaO–MgO–Al_2O_3–SiO_2$ molten slags. ISIJ Int. 2012;52(3):355–62.
31. Zhang GH, Chou KC, Mills K. A structurally based viscosity model for oxide melts. Metall Mater Trans B. 2014;45(2):698–706.
32. Yang XM, Shi CB, Zhang M, Chai G, Wang F. A thermodynamic model of sulfur distribution ratio between $CaO–SiO_2–MgO–FeO–MnO–Al_2O_3$ slags and molten steel during LF refining process based on the ion and molecule coexistence theory. Metall Mater Trans B. 2011;42:1150–80.
33. Yang XM, Shi CB, Zhang M, Duan JP, Zhang J. A thermodynamic model of phosphate capacity for $CaO–SiO_2–MgO–FeO–Fe_2O_3–MnO–Al_2O_3–P_2O_5$ slags equilibrated with molten steel during a top-bottom combined blown converter steelmaking process based on the ion and molecule coexistence theory. Metall Mater Trans B. 2011;42:951–77.
34. Yang XM, Duan JP, Shi CB, Zhang M, Zhang YL, Wang JC. A thermodynamic model of phosphorus distribution ratio between $CaO–SiO_2–MgO–FeO–Fe_2O_3–MnO–Al_2O_3–P_2O_5$ slags and molten steel during a top-bottom combined blown converter steelmaking process based on the ion and molecule coexistence theory. Metall Mater Trans B. 2011;42:738–70.
35. Yang XM, Shi CB, Zhang M, Zhang J. A thermodynamic model for prediction of iron oxide activity in some FeO-containing slag systems. Steel Res Int. 2012;83:244–58.
36. Hou D, Jiang Z, Dong Y, Cao Y, Cao H, Gong W. Thermodynamic design of electroslag remelting slag for high titanium and low aluminium stainless steel based on IMCT. Ironmak Steelmak. 2016;43:517–25.
37. Jiang ZH, Hou D, Dong YW, Cao YL, Cao HB, Gong W. Effect of slag on titanium, silicon, and aluminum contents in superalloy during electroslag remelting. Metall Mater Trans B. 2016;47(2):1465–74.
38. Nafziger R. The system $CaF_2–CaO–Al_2O_3$ under one-third atmosphere of helium. High Temp Sci. 1973;5(6):414–22.